inorganics

MDPI

Article

Exploring the Hydrogen Sorption Capabilities of a Novel Ti-V-Mn-Zr-Nb High-Entropy Alloy

Anis Bouzidi [1], Loïc Perrière [1], Erik Elkaim [2], Laetitia Laversenne [3], Vivian Nassif [3], Gavin Vaughan [4] and Claudia Zlotea [1,*]

[1] Univ Paris Est Creteil, CNRS, ICMPE, UMR 7182, 2 rue Henri Dunant, 94320 Thiais, France
[2] Synchrotron SOLEIL, L'Orme des Merisiers, Saint-Aubin, CEDEX, 91192 Gif sur Yvette, France
[3] University Grenoble Alpes, CNRS, Institut Néel, 38000 Grenoble, France
[4] ESRF-The European Synchrotron, 71, Avenue des Martyrs, CEDEX 9, 38042 Grenoble, France
* Correspondence: claudia.zlotea@cnrs.fr

Abstract: Hydrogen is considered as a clean energy carrier able to achieve the decarbonization of the economy, but its compact, safe, and efficient storage represents an important challenge. Among many materials forming hydrides, this work reports the study of hydrogen sorption properties of a novel *bcc* high-entropy alloy, $Ti_{0.30}V_{0.25}Mn_{0.10}Zr_{0.10}Nb_{0.25}$, synthesized by arc melting. In less than 60 s, the alloy fully absorbs hydrogen at room temperature, reaching a capacity of 2.0 H/M (2.98 wt.%). A two-step reaction with hydrogen is confirmed by pressure-composition isotherms, synchrotron X-ray and neutron diffraction: *bcc* solid solution ↔ *bcc* monohydride ↔ *fcc* dihydride. For the second step transformation, the calculated thermodynamic values indicate the formation of a very stable dihydride, with $\Delta H_{abs} = -97$ kJ/molH_2. Moreover, the pair distribution function analysis of high-energy synchrotron X-ray scattering data validates a completely random distribution of metal atoms in the *fcc* dihydride phase, without noticeable lattice strain nor elemental segregation. In situ synchrotron X-ray and neutron diffraction, performed during hydrogen desorption by heating under vacuum, demonstrated full reversibility of the reaction with hydrogen. On the basis of these results, tuning the chemical composition of high-entropy alloys may have great implications in terms of hydrogen sorption properties.

Keywords: high-entropy alloys; hydrogen storage; in situ synchrotron X-ray diffraction; in situ neutron diffraction; pair distribution function analysis

Citation: Bouzidi, A.; Perrière, L.; Elkaim, E.; Laversenne, L.; Nassif, V.; Vaughan, G.; Zlotea, C. Exploring the Hydrogen Sorption Capabilities of a Novel Ti-V-Mn-Zr-Nb High-Entropy Alloy. *Inorganics* **2023**, *11*, 186. https://doi.org/10.3390/inorganics11050186

Academic Editor: Robert C. Bowman, Jr.

Received: 23 March 2023
Revised: 19 April 2023
Accepted: 24 April 2023
Published: 25 April 2023

1. Introduction

The use of hydrogen as a clean energy carrier has become a viable idea to meet the stringently required decarbonization of the energy sector [1,2]. However, the effective implementation of a full-scale economy of hydrogen requires more efforts to overcome the main technical issue related to hydrogen, i.e., the extreme low density of the dihydrogen gas that limits both the efficient storage and transportation. Pressurized H_2 gas, cryogenic liquid, and physically/chemically bonded hydrogen to solid-state materials are the current existing ways for hydrogen storage [3,4]. Nevertheless, storing hydrogen in the form of either gaseous or liquid states presents many disadvantages, such as, high cost, large volume tanks, and safety issues. Hydrogen storage in metals and metallic alloys is a clean, safe, and efficient alternative only if the following characteristics are fulfilled: high absorption capacities, reaction close to ambient pressure and temperature, fast kinetics, and good cycling stability.

Many metals and metallic alloys have been studied for their hydrogen sorption properties and depending on the nature of elements and their concentrations in the material, the properties may change remarkably [5]. The search for the right combination of elements and their optimal stoichiometry to fulfill all the above-mentioned features is a

great challenge. Many metallic materials are currently being studied for hydrogen storage. For example, LaNi5 and TiFe intermetallic compounds present good hydrogen storage reversibility, but they are disadvantaged either by the low storage capacities, activation difficulties, or the high price of raw materials [6–8]. Along with intermetallics, alloys are promising candidates to find the most efficient material for hydrogen storage applications. Traditionally, the alloying strategy consists of the addition of several elements in small amounts within one or two main elements to obtain compositions with enhanced properties. Along with conventional alloys, another metallurgic paradigm was proposed in 2004 based on the mixing of at least five elements near equimolar composition (concentration of each element is between 5 to 35 at.%) [9,10]. These materials are defined as high-entropy alloys (HEA) and have been initially proposed for their interesting mechanical properties [11,12]. Interestingly, HEAs are known to adopt simple crystalline structures, such as body-centered cubic (*bcc*), face-centered cubic (*fcc*), and hexagonal close compact (*hcp*). In such simple crystalline structures, the mixing of elements with different atomic radii might result in an important lattice distortion with possibly large interstitial sites that might facilitate the hydrogen insertion and increase the amount of stored hydrogen. The lattice distortion is described by the empirical parameter δ, defined elsewhere [13]. Additionally, another empirical parameter is the valence electron concentration, VEC, which is described by the number of valence electrons per formula unit [14]. Presently, *bcc* HEAs containing refractory elements are studied for solid-state hydrogen storage applications due to their interesting properties and large chemical versatility (the nature, the number, and the concentration of elements can be tuned) [15–18].

In this framework, the series of *bcc* HEAs $Ti_{0.30}V_{0.25}Zr_{0.10}Nb_{0.25}M_{0.10}$ (*M* = Mg, Al, Cr, Mo, and Ta) [19–23] has been thoroughly studied in our group to explore the effect of the addition of 10 at.% of a fifth *M* element into the quaternary alloy $Ti_{0.325}V_{0.275}Zr_{0.120}Nb_{0.275}$ [24]. The hydrogen capacity is affected by the nature of the *M* element: the quaternary alloy can absorb 2.5 wt.% hydrogen, whereas the capacities are 2.5, 2.6, 2.7, 2.8, and 3.0 wt.% after adding 10 at.% of Ta, Al, Mg, Mo, and Cr, respectively [19–23]. Furthermore, the hydrogen desorption properties are also optimized after the addition of the fifth element, mainly for compositions containing Al, Ta, and Cr. Following these studies, a relationship between the VEC and the storage capacity has been proposed in this series of HEAs [25]. For a VEC < 4.9, the capacity of absorption is in the range of 1.5–2.0 H/M, whereas for HEAs with a VEC $\geq$ 4.9, the capacity of hydrogen absorption drastically decreases. In light of these findings, the $Ti_{0.30}V_{0.25}Mn_{0.10}Zr_{0.10}Nb_{0.25}$ with VEC = 4.8 shows one of the best capacities (2.0 H/M or 2.98 wt.%). Therefore, the aim of the present work is to thoroughly investigate the composition $Ti_{0.30}V_{0.25}Mn_{0.10}Zr_{0.10}Nb_{0.25}$, with a focus on the structure, the microstructure, the chemical homogeneity, the hydrogen sorption properties, and the phase transition during the reversible hydrogenation reaction. Regarding the latter aspect, both ex situ and in situ characterizations using neutrons and synchrotron radiation have been carried out to analyze both the average and local crystalline structures of different phases.

2. Results and Discussion

The calculated empirical parameters for the composition $Ti_{0.30}V_{0.25}Mn_{0.10}Zr_{0.10}Nb_{0.25}$ are δ = 5.7% and VEC = 4.8, based on the definitions proposed elsewhere [13]. Compared to the quaternary alloy $Ti_{0.325}V_{0.275}Zr_{0.120}Nb_{0.275}$, the δ decreases from 6% to 5.7% after the addition of Mn. This could be explained by the fact that the Mn radius is close to the values of the other constituent elements (r_V = 1.31 Å < r_{Mn} = 1.37 Å < r_{Nb} = 1.43 Å < r_{Ti} = 1.45 Å < r_{Zr} = 1.59 Å as taken from [26]) and it results in the reduction of the atomic size disparity. The VEC increases from 4.55 to 4.8 after the addition of Mn to the quaternary alloy.

The $Ti_{0.30}V_{0.25}Mn_{0.10}Zr_{0.10}Nb_{0.25}$ alloy crystallizes in a single *bcc* ($Im\bar{3}m$) structure (see laboratory XRD in Figure 1A), with a lattice parameter a_{bcc} = 3.239(5) Å, which is close to a_{bcc}= 3.261(1) Å, previously obtained for the quaternary alloy $Ti_{0.325}V_{0.275}Zr_{0.120}Nb_{0.275}$ [24]. Figure 1B displays the SEM-EDS chemical mapping results of the as-cast $Ti_{0.30}V_{0.25}Mn_{0.10}Zr_{0.10}Nb_{0.25}$. A dendritic morphology can be noticed, similarly to previ-

ously reported refractory HEAs synthesized by arc melting [21,22,27]. The results of the EDS chemical analysis are listed in Table 1, proving a good agreement between the overall and the nominal compositions.

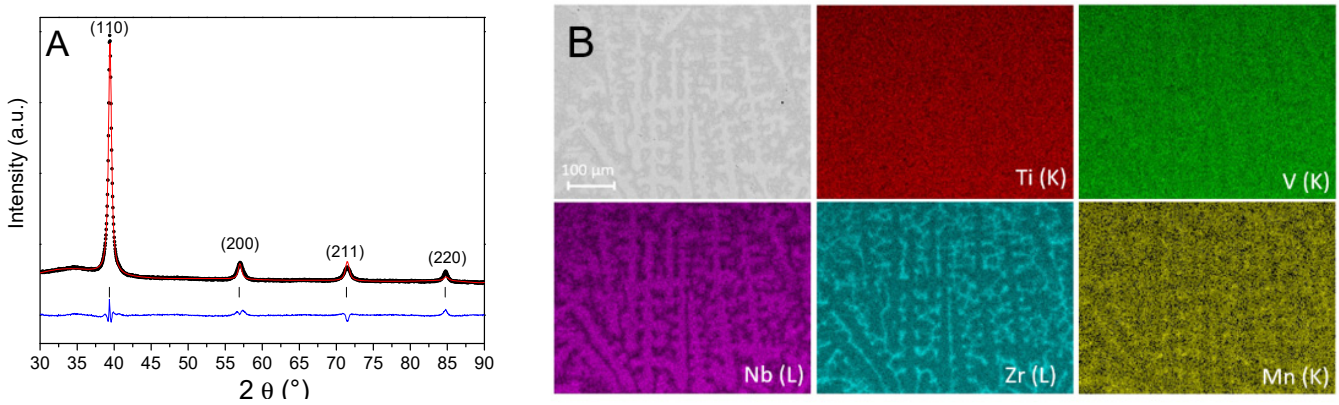

Figure 1. (**A**) X-ray diffraction pattern (λ = 1.5406 Å) and corresponding structural refinement, and (**B**) the scanning electron microscopy image and energy-dispersive X-ray spectroscopy (SEM-EDS) chemical mapping of the as-cast $Ti_{0.30}V_{0.25}Mn_{0.10}Zr_{0.10}Nb_{0.25}$ alloy.

Table 1. Chemical composition of the dendritic and interdendritic regions, as well as the overall values for the as-cast $Ti_{0.30}V_{0.25}Mn_{0.10}Zr_{0.10}Nb_{0.25}$ alloy.

Region	Ti (at.%)	V (at.%)	Mn (at.%)	Zr (at.%)	Nb (at.%)
Dendritic	29.4 (0.2)	24.4 (0.8)	11.5 (1.3)	6.5 (1.2)	28.2 (1.8)
Interdendritic	30.2 (0.6)	25.5 (0.9)	8.1 (1.2)	15.5 (1.8)	20.7 (1.5)
Overall	29.9 (0.5)	24.9 (0.6)	9.5 (1.0)	10.5 (1.2)	25.2 (1.1)
Nominal	30	25	10	10	25

The dendritic regions are enriched mainly by Nb and slightly by Mn, whereas the interdendritic regions are rich in Zr, Ti, and V, and are close to the nominal compositions, irrespective of the areas. The Nb enrichment of dendritic zones can be explained by the difference of the melting temperatures between the constituent elements. During the solidification process, a Nb-rich solid phase (dendrite) is formed in the beginning because of the higher melting temperature of Nb as compared to the other elements, whereas a liquid phase poor in Nb will later form the interdendritic areas. This microstructure is commonly encountered in refractory HEAs synthesized by high-temperature arc melting and usually has no influence on hydrogen sorption properties [21,22,27,28].

The structural and microstructural characterizations demonstrate that this composition is a single-phase *bcc* alloy with typical dendritic microstructure. Thus, the next section is dedicated to the study of the hydrogen sorption properties, such as kinetics of absorption, thermodynamics of the reaction with hydrogen, structure investigation of hydride phases, and the phase transformation pathway.

The kinetics of hydrogen absorption was acquired at 25 °C under 44 bars of hydrogen pressure (Figure 2A), after an activation step described in the "Materials and Methods" section. This curve shows extremely fast kinetics of absorption, with 95% of the maximum absorbed capacity reached within 30 s. The maximum capacity of absorption is 2.0 H/M (2.98 wt.%), which is higher than 1.7 H/M (2.5 wt.%) obtained for the quaternary alloy [24] and comparable to the maximum uptakes already reported for Ti, V, Zr, and Nb elemental hydrides [29]. Moreover, the capacity obtained for $Ti_{0.30}V_{0.25}Mn_{0.10}Zr_{0.10}Nb_{0.25}$ perfectly matches the values from similar compositions, such as $Ti_{0.30}V_{0.25}Zr_{0.10}Nb_{0.25}M_{0.10}$, with *M* = Cr [21], Mo [22], and Ta [25]. The dihydride and the corresponding deuterated phases were characterized by SR-XRD (Figure 2B) and neutron diffraction (Figure 2C), respectively. The related Rietveld analyses of the diffraction patterns confirm that the

dihydride adopts a *fcc* structure ($Fm\bar{3}m$) with a lattice parameter listed in Table 2. However, a small amount of secondary phase, possibly the *bcc* monohydride phase, is present in the neutron diffraction pattern (star symbols in Figure 2C). Rietveld refinement on neutron diffraction data confirms that the deuterium (hydrogen) atoms occupy the tetrahedral sites of the *fcc* structure (1/4, 1/4, 1/4), in good agreement with previous findings for similar HEAs [19,21,22,30].

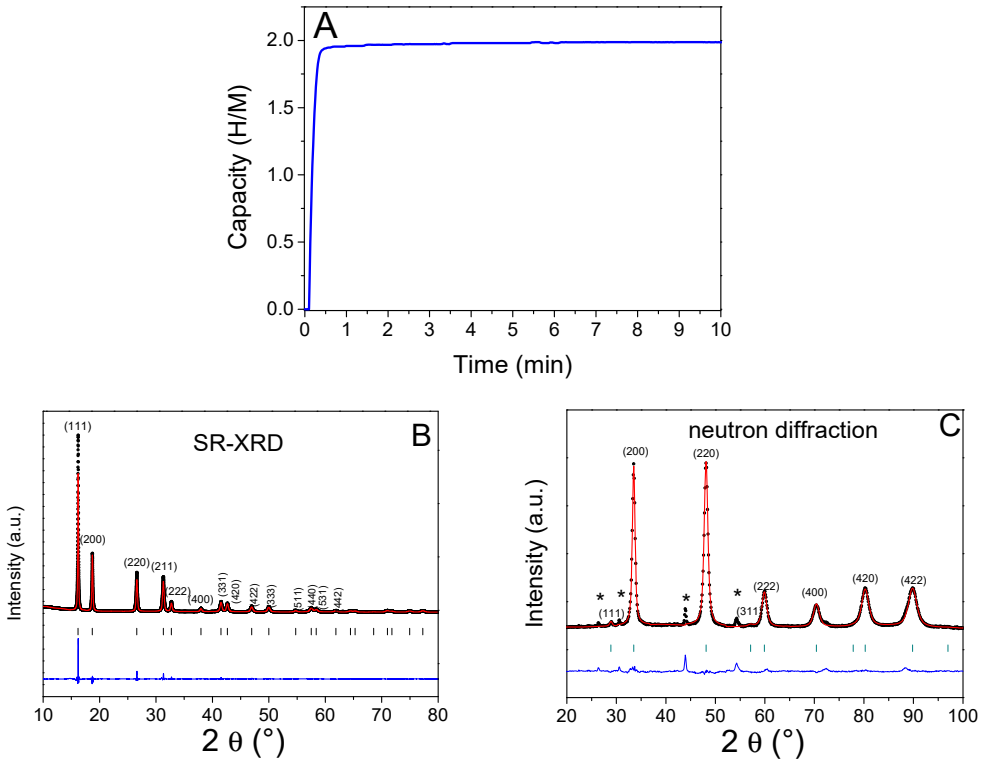

Figure 2. Kinetics of hydrogen absorption at 25 °C under 44 bar H_2 pressure (**A**); SR-XRD pattern (λ = 0.7289 Å) of the dihydride $Ti_{0.30}V_{0.25}Mn_{0.10}Zr_{0.10}Nb_{0.25}H_2$ and related Rietveld analysis (**B**); neutron diffraction diagram (λ = 1.2858 Å) of the deuteride $Ti_{0.30}V_{0.25}Mn_{0.10}Zr_{0.10}Nb_{0.25}D_2$ and corresponding Rietveld analysis (**C**). The star symbols indicate the presence of a minor secondary phase only visible by neutron diffraction.

Table 2. The *fcc* lattice parameter of the $Ti_{0.30}V_{0.25}Mn_{0.10}Zr_{0.10}Nb_{0.25}H(D)_2$ from SR-XRD (CRISTAL SOLEIL), neutron diffraction (D1B ILL), and PDF analysis (ID15 ESRF). The isotropic atomic displacement parameter (U_{iso}) obtained from PDF modeling is also given.

Sample	*fcc* Lattice Parameter, a_{fcc} (Å)			U_{iso} (Å^2)
	SR-XRD	Neutron Diffraction	PDF	PDF
$Ti_{0.30}V_{0.25}Mn_{0.10}Zr_{0.10}Nb_{0.25}\mathbf{H_2}$	4.482 (1)	-	4.485 (1)	0.009 (1)
$Ti_{0.30}V_{0.25}Mn_{0.10}Zr_{0.10}Nb_{0.25}\mathbf{D_2}$	-	4.460 (2)	-	-

To determine the thermodynamic properties of a reaction with hydrogen, i.e., the enthalpy and entropy of dihydride formation, several pressure-composition isotherms were measured at 25, 227, 255, and 280 °C, and the Van't Hoff method was applied on the three data obtained at high temperature only (Figure 3). A two-step reaction with hydrogen is observed in the PCI curves recorded at high temperature, whereas at 25 °C, this behavior is not noticeable due to the low equilibrium pressure values (within the error bar of the pressure transducer). A first transition occurs at a very low pressure (below the minimum measurable value of the pressure transducer), resulting in the formation of a monohydride

phase with a capacity of around 1 H/M. A second reaction arises at a higher pressure, forming a dihydride phase (2 H/M) with a very sloped plateau. This two-step behavior is similar to the hydrogen absorption reaction observed for $Ti_{0.30}V_{0.25}Cr_{0.10}Zr_{0.10}Nb_{0.25}$ [21], and contrasts the one-step transition noticed for $Ti_{0.30}V_{0.25}Zr_{0.10}Nb_{0.25}Mo_{0.10}$ [22]. This highlights the importance of the nature of the fifth element added in the pristine quaternary alloy $Ti_{0.325}V_{0.275}Zr_{0.120}Nb_{0.275}$ [24].

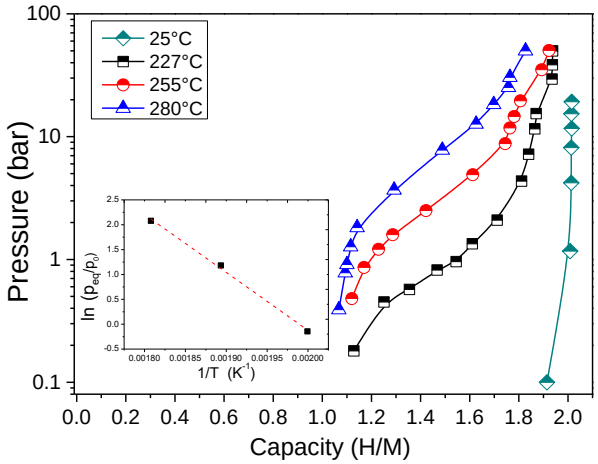

Figure 3. Pressure-composition isotherms of the $Ti_{0.30}V_{0.25}Mn_{0.10}Zr_{0.10}Nb_{0.25}$ alloy at 25, 227, 255, and 280 °C. Inset: Van't Hoff plot applied on data obtained at a high temperature.

With the increase in temperature from 227 to 280 °C, the equilibrium pressure of the second transition increases, which allows for the calculation of the variation of the enthalpy (ΔH_{abs}) and the entropy (ΔS_{abs}) (Table 3). The modulus value of the enthalpy is quite large, suggesting the formation of a very stable dihydride. However, the entropy value is larger than the expected value of H_2 gas entropy, -130 J/K·molH_2. Two reasons might be invoked to explain this behavior: the slopping nature of the PCI measurements and the short range of the PCI temperatures (from 227 to 280 °C). The first reason makes the determination of mid-plateau values difficult, whereas the second one may introduce errors in the linear regression of the Van't Hoff plot.

Table 3. Thermodynamic properties for dihydride formation in $Ti_{0.30}V_{0.25}Mn_{0.10}Zr_{0.10}Nb_{0.25}$, as determined by Van't Hoff analysis. ΔH_{abs} and ΔS_{abs} of other similar alloys are also listed.

Composition	ΔH_{abs} (KJ/molH_2)	ΔS_{abs} (J/KmolH_2)	Reference
$Ti_{0.30}V_{0.25}Mn_{0.10}Zr_{0.10}Nb_{0.25}$	−97 (±5)	−193 (±9)	Present work
$Ti_{0.30}V_{0.25}Cr_{0.10}Zr_{0.10}Nb_{0.25}$	−75 (±4)	−161 (±8)	[21]
$(TiVNb)_{0.85}Cr_{0.15}$	−67 (±2)	−172 (±4)	[28]
$(TiVNb)_{0.953}Co_{0.047}$	−67 (±2)	−174 (±5)	[28]
TiVNb	−67 (±5)	−157 (±11)	[31]

For the sake of comparison, the enthalpy and entropy of hydrogen absorption in other refractory HEAs are also listed in Table 3. It is obvious that the Mn addition in this series of alloys is responsible for the formation of a very stable dihydride phase, which is more stable than the related Cr-containing composition ($Ti_{0.30}V_{0.25}Cr_{0.10}Zr_{0.10}Nb_{0.25}$) or other HEAs [21].

An investigation of the local structure of $Ti_{0.30}V_{0.25}Mn_{0.10}Zr_{0.10}Nb_{0.25}H_2$ at short- and medium-range order was carried out using X-ray total scattering and related pair distribution function (PDF) analysis, using the G(R) formalism. The local structure of the hydride in terms of the real-space distribution of interatomic distances is shown from the PDF profile in Figure 4 together with the corresponding refinement, using an average *fcc*

lattice with a random distribution of metallic atoms. The refinement results for the *fcc* lattice parameter and the isotropic atomic displacement parameter (U_{iso}) are given in Table 2. A good agreement is observed between the values of the lattice parameters obtained by SR-XRD and PDF.

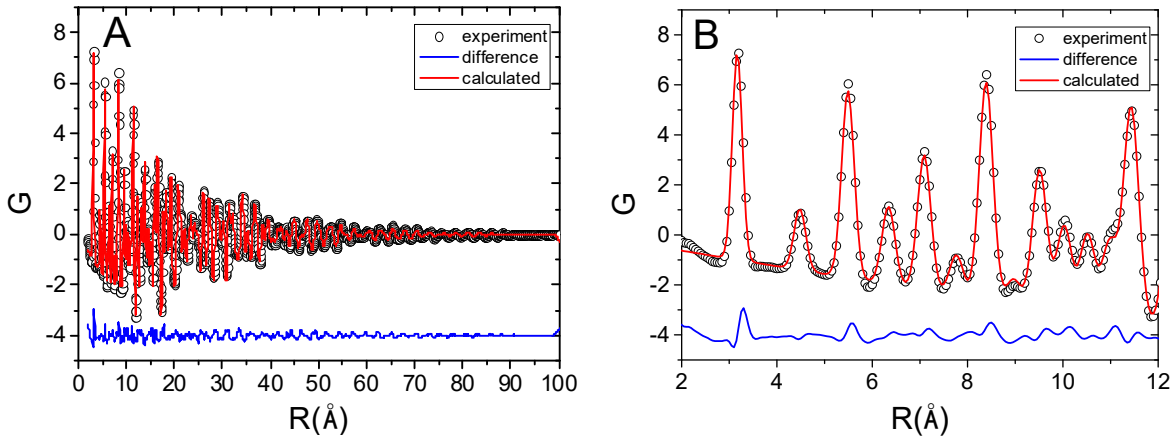

Figure 4. X-ray PDF profile for the $Ti_{0.30}V_{0.25}Mn_{0.10}Zr_{0.10}Nb_{0.25}H_2$ dihydride and the corresponding refinement based on a *fcc* random structure in the whole R range (**A**) and in the low R region (**B**).

The difference curve between the experimental and the calculated profiles suggests that the medium structure (high R region) and the local structure (low R range) can be well described by an undistorted random *fcc* lattice. All observed features in the PDF data are well explained by an average random *fcc* structure without any sign of strong lattice distortion at a short range order or elemental segregation. Recently, it has been demonstrated by combined X-ray and neutron PDF analysis that the lattice distortion initially present in as-cast refractory *bcc* alloys can be relieved by the formation of dihydrides with an *fcc* lattice [32]. Previously, we have reported the PDF profiles for two related dihydrides: $Ti_{0.325}V_{0.275}Zr_{0.125}Nb_{0.275}H_{1.7}$ and $Ti_{0.30}V_{0.25}Zr_{0.10}Nb_{0.25}Mo_{0.10}H_2$ [22]. These PDF profiles are very similar to the present one, hinting to the same local order. This might be understood by the comparable crystalline structure (*fcc*) and close chemical compositions (90% of atoms are identical).

Based on PCIs, SR-XRD, neutron diffraction and PDF results, the hydrogen absorption follows a two-step reaction: from the as-cast alloy to an intermediate monohydride at a low pressure and subsequently, to a dihydride phase at higher pressures. The same sequence has been already reported for other refractory HEAs, such as $Ti_{0.30}V_{0.25}Cr_{0.10}Zr_{0.10}Nb_{0.25}$ [21], TiVNb, and $Al_{0.10}Ti_{0.30}V_{0.30}Nb_{0.30}$ [31]. Therefore, it is important to investigate the crystalline structure as a function of hydrogen content. Several samples with different hydrogen absorption capacities, such as 2.0 H/M, 0.8 H/M, 0.5 H/M, and a fully desorbed sample (0 H/M), were studied by X-ray diffraction (laboratory XRD and SR-XRD), as displayed in Figure 5. The refined lattice parameters and phase fractions are listed in Table 4.

The dihydride phase crystallizes in an *fcc* lattice, as previously demonstrated by several experimental methods, whereas the intermediate monohydride with 0.8 H/M is a *bcc* single phase with a_{bcc} = 3.340 (6) Å, which is larger than a_{bcc} = 3.239 (5) Å of the as-cast alloy. The material with 0.5 H/M consists of a mixture of two *bcc* phases: one is the monohydride phase with a slightly smaller lattice parameter (a_{bcc} = 3.261 (1) Å and phase abundance: 54%) and the second one is a *bcc* solid solution with hydrogen (a_{bcc} = 3.243 (1) Å and phase abundance: 46%).

The completely desorbed sample has the same *bcc* lattice as the as-cast sample, without any sign of phase segregation, but with a slightly larger lattice parameter a_{bcc} = 3.251 (2) Å than the pristine as-cast alloy a_{bcc} = 3.239 (5) Å. This discrepancy might be accounted for by an uncomplete hydrogen desorption under the present experimental conditions.

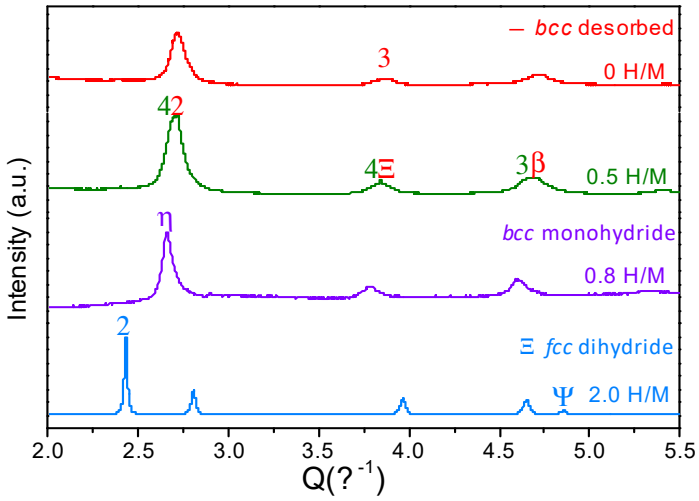

Figure 5. XRD patterns of $Ti_{0.30}V_{0.25}Mn_{0.10}Zr_{0.10}Nb_{0.25}$ with different hydrogen capacities: 2.0 H/M, 0.8 H/M, 0.5 H/M, and 0 H/M (desorbed).

Table 4. Lattice parameters and phase fractions of $Ti_{0.30}V_{0.25}Mn_{0.10}Zr_{0.10}Nb_{0.25}$ with different hydrogen absorption capacities.

Hydrogen Capacity	Lattice Parameter (Å)			Phase Fraction (%)		
	fcc Dihydride	*bcc* Monohydride	*bcc* Solid Solution	*fcc* Dihydride	*bcc* Monohydride	*bcc* Solid Solution
2.0 H/M	4.482(1)	-	-	100	-	-
0.8 H/M	-	3.340 (6)	-	-	100	-
0.5 H/M	-	3.261 (5)	3.243 (5)	-	54	46
0.0 H/M	-	-	3.251 (2)	-	-	100

Further investigation of the reversibility of hydrogen/deuterium desorption in $Ti_{0.30}V_{0.25}Mn_{0.10}Zr_{0.10}Nb_{0.25}$ was carried out using in situ neutron diffraction. The diffraction patterns have been recorded for the deuteride $Ti_{0.30}V_{0.25}Mn_{0.10}Zr_{0.10}Nb_{0.25}D_2$ phase during heating from 40 to 450 °C, with a temperature rate of 1 °C/min under dynamic vacuum (Figure 6).

Starting from the bottom to the top of Figure 6 (left), the initial *fcc* deuteride phase (marked with #) is stable until a sharp transition occurs in the temperature range 240–320 °C, with a maximum desorption rate at 280 °C. The deuteride *fcc* phase abruptly disappears at 280 °C due to deuterium desorption and only weak diffraction peaks (marked with *) from the *bcc*-desorbed phase are barely visible. This is due to the low thermal neutron cross section of the desorbed alloy, as also reported for the quaternary $Ti_{0.325}V_{0.275}Zr_{0.125}Nb_{0.275}$ alloy. The latter composition undergoes a similar sharp transition due to deuterium desorption in a single event, at around 270 °C [23]. The very close desorption temperatures noticed by in situ neutron thermo-diffraction hints to a negligible effect of Mn addition on the deuterium desorption properties. This finding is in contrast with the results of the additions of 10 at.% of Al, Cr, and Ta in the quaternary alloy that have proven to significantly lower the desorption temperature [21,23].

A structural analysis of the *bcc* desorbed phase cannot be exploited from in situ neutron diffraction due to very weak diffraction peaks in the absence of deuterium. Thus, for an in-depth investigation of the phase transition during the desorption, in situ SR-XRD patterns were analyzed starting from the dihydride $Ti_{0.30}V_{0.25}Mn_{0.10}Zr_{0.10}Nb_{0.25}H_2$ (Figure 7).

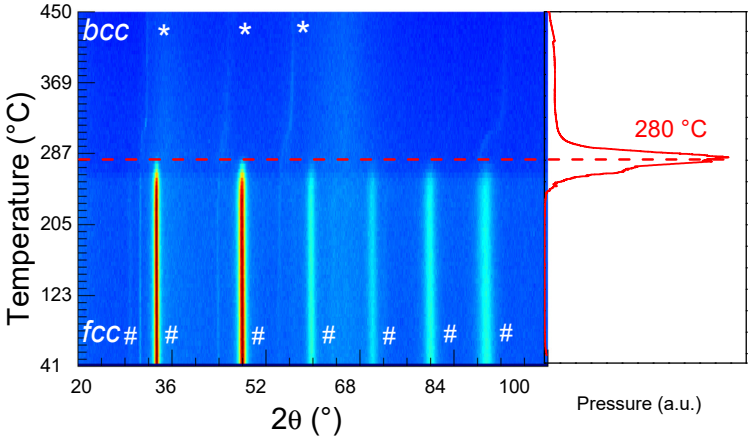

Figure 6. In situ neutron diffraction during deuterium desorption from $Ti_{0.30}V_{0.25}Mn_{0.10}Zr_{0.10}Nb_{0.25}D_2$ (λ = 1.28 Å), with a heating rate of 1 °C/min from 40 to 450 °C under dynamic vacuum (**left**) and the corresponding gas desorption profile (**right**).

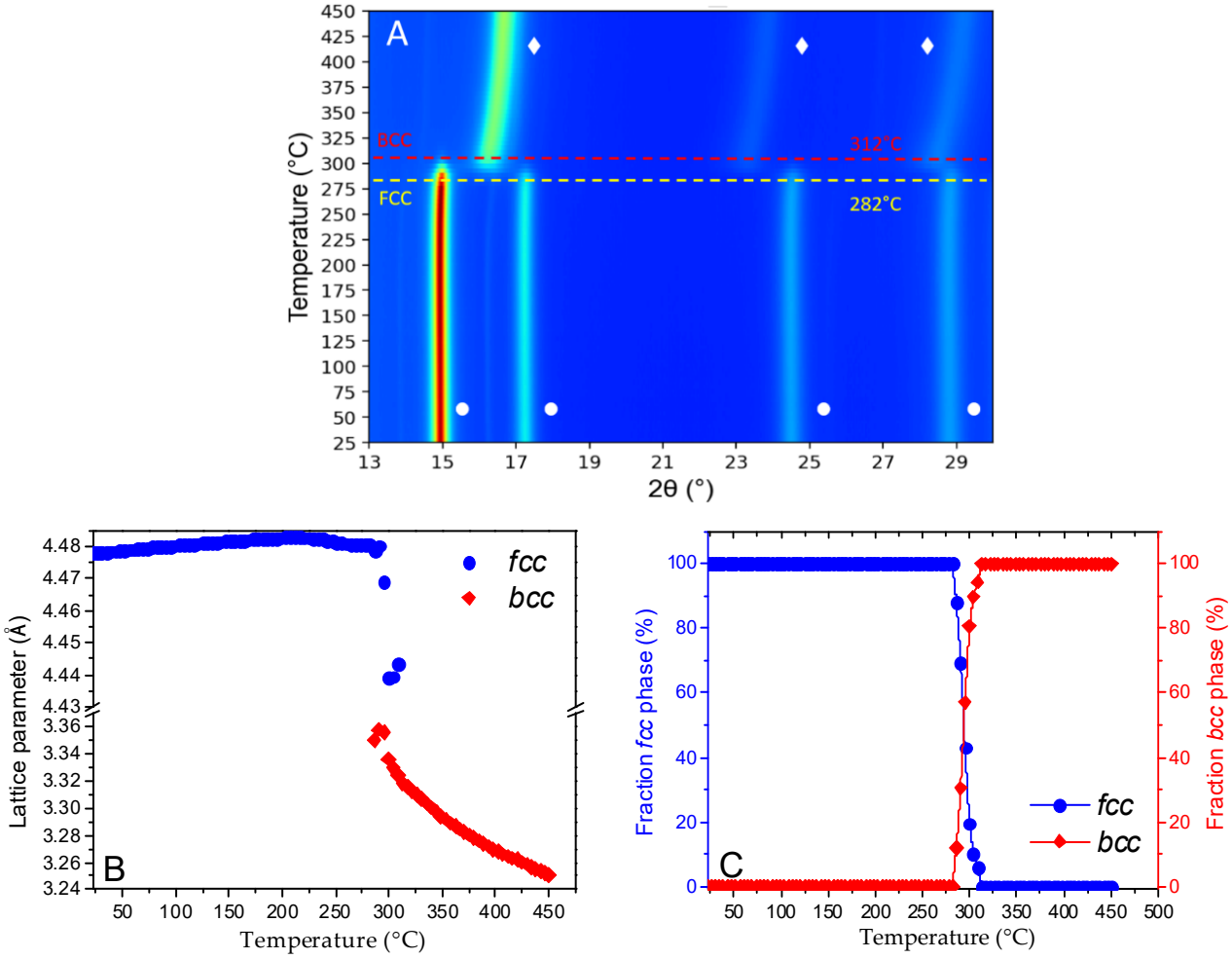

Figure 7. (**A**) In situ SR-XRD (λ = 0.67156 Å) of $Ti_{0.30}V_{0.25}Mn_{0.10}Zr_{0.10}Nb_{0.25}H_2$ dihydride during heating from 25 to 450 °C (5 °C/min) under dynamic vacuum. (**B**) The variation of the lattice parameter of the *fcc* and *bcc* phases versus temperature. (**C**) The thermal evolution of the *fcc* and *bcc* phase fractions.

Figure 7A shows in situ SR-XRD thermo-diffractograms during the hydrogen desorption from the dihydride $Ti_{0.30}V_{0.25}Mn_{0.10}Zr_{0.10}Nb_{0.25}H_2$, while heating from 25 to 450 °C

under dynamic vacuum (5 °C/min). The *fcc* dihydride phase (marked with white circles) is stable up to around 275 °C. Above this temperature, the dihydride undergoes a sharp transition to a *bcc*-desorbed phase (marked with diamond symbols), in very good agreement with in situ neutron diffraction data. Rietveld analysis was applied to gain in-depth information on the phase transition: the thermal variation of lattice parameters and phase fractions are illustrated in Figure 7B,C, respectively. A thermal expansion of the *fcc* lattice parameter from 4.478 (1) Å to 4.482 (1) Å is noticed upon a temperature increase from 25 to around 211 °C (Figure 7B). Above this temperature, the lattice parameter slightly decreases due to the beginning of the hydrogen desorption. In the 282–312 °C range, a progressively vanishing *fcc* dihydride coexists with a newly formed *bcc* phase. The lattice parameter of the dihydride *fcc* phase strongly decreases from 4.482 (1) Å to 4.443 (1) Å, and the phase fraction diminishes from 100 to 6% (Figure 7C). Above 312 °C, only the desorbed *bcc* phase is visible with the lattice parameter continuously decreasing from 3.318 (1) Å to 3.250 (1) Å at the maximum temperature of 450 °C. This value is slightly larger than 3.239 (5) Å for the as-cast alloy that might be described by thermal expansion.

Intriguingly, both in situ SR-XRD and neutron diffraction experiments hint to a single step desorption (*fcc* dihydride → *bcc* phase), whereas the PCIs and ex situ XRD at different hydrogen concentrations have demonstrated a two-step reaction with hydrogen: *fcc* dihydride ↔ *bcc* monohydride ↔ *bcc* desorbed phase. The second transition from *bcc* monohydride to a completely desorbed *bcc* phase could not be detected by in situ SR-XRD. One possible explanation might be based on the very small displacive rearrangement of atoms involved into the transition from the *bcc* monohydride to the *bcc* solid solution, as already observed for the closely related alloy Ti-V-Cr-Zr-Nb [21]. However, the in situ experiments clearly demonstrated full reversibility, suggesting a structurally stable alloy during the absorption/desorption cycling of hydrogen.

3. Materials and Methods

The $Ti_{0.30}V_{0.25}Mn_{0.10}Zr_{0.10}Nb_{0.25}$ alloy was prepared by high-temperature arc melting under Ar atmosphere to avoid any contaminations, as described previously [25]. This is the most widespread method to prepare refractory HEAs [27]. The samples as both coarse and fine powders can be manipulated in air without any pyrophoric risk. However, they are stored into an Ar glove box to minimize the air exposure and surface oxidation.

The microstructure of the as-cast alloy was analyzed with a scanning electron microscopy (SEM), using a Zeiss Merlin microscope. Furthermore, energy dispersive X-ray spectroscopy (EDS) was used for the chemical mapping. Prior to the analysis, the sample was exposed to air for at least 24 h, in order to be immobilized in an epoxy resin, polished and finally coated with 1.9 nm of Pd, as already reported for the SEM-EDS analysis of HEAs [33–35].

The crystalline structure of the materials in different forms (as-cast, hydride, desorbed, etc.) was studied via X-ray powder diffraction (XRD), using both a laboratory X-ray diffractometer D8 advance Bruker (Cu K_α radiation, Bragg-Brentano geometry) and synchrotron radiation measurements (SR-XRD) at the CRISTAL beamline in the SOLEIL facility. The powder samples were handled and measured in air for all ex situ experiments. Ex situ (λ = 0.7289 Å) and in situ (λ = 0.67156 Å) SR-XRD diagrams were recorded using the Mythen2 detector system (Dectris Ltd., Switzerland installed on the powder diffractometer. To minimize X-ray absorption during the in situ experiment, the sample was mixed with a fumed silica powder and enclosed in 0.2 mm diameter quartz capillary tube. The powder mixture was manipulated and loaded into the quartz capillary under air, with a limited time exposure. For ex situ measurements, the powder samples were loaded and measured in glass capillaries in air.

During the hydrogen desorption from the hydride phase, the SR-XRD patterns were recorded while applying a constant temperature ramp (5 °C/min) from 25 to 450 °C under dynamic secondary vacuum. These in situ measurements were acquired with a

3 min/pattern acquisition time in the 0.2 to 65° 2θ range. The time of acquisition was 10 min, with a scanning range from 1° to 85° (2θ) for these ex situ experiments.

High-energy synchrotron XRD measurements on the powder hydride phase were carried out at beamline ID15A at ESRF, Grenoble (France) [36]. The incident flux was normalized using a diode placed in front of the sample. Diffraction patterns were collected in transmission geometry by using a Pilatus3 X CdTe 2M hybrid photon-counting detector. The powder sample was handled and loaded into a glass capillary under air. A number of diffraction patterns were collected at slightly different detector positions, in order to minimize inhomogeneity effects and cover dead zones. The detector was off-centered with respect to the 99 keV incident beam and positioned close to the sample to access Q values of up to ~30 $Å^{-1}$. The images were corrected for detector geometry, response, distortion, transparency, and for background contributions and X-ray polarization. Data were azimuthally integrated using a modified version [37] of the PyFAI library [38] to give one-dimensional scattering patterns. The G(r) were calculated from these patterns using routines from the Diffpy-CMI library [39] with local modifications for outlier rejection and treatment of background. The structural analysis was carried out using the PDFgui free software [40].

Powder neutron diffraction experiments on deuterated samples were performed at the D1B beamline at the Institute Laue-Langevin (λ = 1.2858 Å) (DOI: 10.5291/ILL.DATA.CRG-2768), in the scanning range from 1 to 128° (2θ). At room temperature, the ex situ measurement was carried out on a vanadium container, whereas for the in situ measurements, the sample was placed in a silica tube. The powder samples have been manipulated and loaded into the respective containers under air with a limited time exposure. The recording of the diffraction patterns was carried out during the desorption of the deuterated powder sample by applying constant heating (1 °C/min) under secondary vacuum. The evolution of the pressure of evolved gas was continuously recorded by a vacuum gauge during the desorption experiment.

The refinement of the collected neutron and SR powder diffraction data was carried out using the Rietveld method with the Fullprof software [41], whereas the fundamental parameters approach [42], as implemented in the TOPAS program (Bruker AXS version 7.0.0.7) [43], was used to refine the laboratory X-ray diffraction patterns.

Hydrogen sorption properties were studied using a homemade volumetric device, water thermalized at 25 °C. Small pieces of the as-cast alloy (300–400 mg) were cut and loaded under air in a stainless-steel container, with an air exposure of less than 10 min. The stainless-steel container with a minimized dead volume was tightly connected to the volumetric device by a single-use metallic gasket, and a leak test was performed before any activation of the sample. Prior to each experiment, the samples were activated by a heat treatment at 350 °C under a dynamic vacuum for 3 h. The hydrogen uptake was calculated using the real equation of states for hydrogen from the program GASPAK V3.32 (Cryodata. Inc., USA). The absorption kinetic curve was recorded during a first absorption step, under 44 bars of H_2 at room temperature (25 °C). Pressure-composition isotherms (PCI) at 25, 227, 255, and 280 °C have been acquired during absorption and further used to calculate the enthalpy and entropy of the reaction using the Van't Hoff method. During the PCI measurements, each point was in equilibrium and the minimum time per point was around 6 h. Furthermore, these measurements were conducted following the recommended best practices from Gross et al. [44], and with careful consideration of the potential limiting factors that could affect the repeatability of the results previously outlined by Broom et al. [45].

4. Conclusions

A novel high-entropy alloy $Ti_{0.30}V_{0.25}Mn_{0.10}Zr_{0.10}Nb_{0.25}$ was successfully synthesized by high-temperature arc melting to form a homogeneous *bcc* single phase. This alloy absorbs hydrogen very quickly at room temperature, reaching a full dihydride phase in less than 60 s. An improved hydrogen sorption capacity of 2.0 H/M (2.98 wt.%) is found for this quinary

alloy as compared to the quaternary composition $Ti_{0.325}V_{0.275}Zr_{0.120}Nb_{0.275}$ (without Mn) that absorbs 1.7 H/M (2.5 wt.%). Moreover, the $Ti_{0.30}V_{0.25}Mn_{0.10}Zr_{0.10}Nb_{0.25}$ composition undergoes a reversible two-step reaction with hydrogen: *bcc* ↔ *bcc* monohydride ↔ *fcc* dihydride. The thermodynamics of the second reaction uncovered the formation of the most stable dihydride in this series of alloys $Ti_{0.30a}V_{0.25}Zr_{0.10}Nb_{0.25}M_{0.10}$. This finding corroborates the strategy that small changes (10 at.%) in the chemical composition of high-entropy alloys may have tremendous implications in terms of hydrogen sorption properties. Thus, tuning the chemistry is crucial to design materials with promising hydrogen sorption properties.

Author Contributions: Conceptualization, C.Z.; methodology, A.B., L.P., L.L., V.N., E.E., G.V. and C.Z.; validation, A.B., L.P., L.L., V.N., E.E., G.V. and C.Z.; formal analysis, A.B. and C.Z.; investigation, A.B., L.L., V.N., E.E., G.V. and C.Z.; data curation, C.Z.; writing—original draft preparation, A.B. and C.Z.; writing—review and editing, A.B., L.L., V.N., E.E., G.V. and C.Z.; supervision, C.Z.; funding acquisition, C.Z. All authors have read and agreed to the published version of the manuscript.

Funding: This work was financially supported by the French National Research Agency (ANR) within the framework of the MASSHY project (ANR-19-CE05-0029-01).

Data Availability Statement: The data presented in this study are available on request from the corresponding author.

Acknowledgments: C.Z. and A.B. would like to thank Valérie Lalanne, Olivier Rouleau, Benjamin Villeroy, and Rémy Pires from ICMPE for their technical support during this project. Sofien Djellit from ILL and Fabrice Couturas from ICMPE are acknowledged for their help with neutron diffraction at ILL. We acknowledge the beamtime allocation and financial support from the French Federation of Neutron Scattering (2FDN). This work has been accepted for synchrotron beamtime by the Soleil scientific on the CRISTAL beamline (proposal 20210367).

Conflicts of Interest: The authors declare no conflict of interest.

References

1. Abe, J.O.; Popoola, A.P.I.; Ajenifuja, E.; Popoola, O.M. Hydrogen Energy, Economy and Storage: Review and Recommendation. *Int. J. Hydrogen Energy* **2019**, *44*, 15072–15086. [CrossRef]
2. Eberle, U.; Felderhoff, M.; Schuth, F. Chemical and Physical Solutions for Hydrogen Storage. *Angew. Chem.-Int. Ed.* **2009**, *48*, 6608–6630. [CrossRef] [PubMed]
3. Veziroğlu, T.N.; Şahi¨n, S. 21st Century's Energy: Hydrogen Energy System. *Energy Convers. Manag.* **2008**, *49*, 1820–1831. [CrossRef]
4. Allendorf, M.D.; Stavila, V.; Snider, J.L.; Witman, M.; Bowden, M.E.; Brooks, K.; Tran, B.L.; Autrey, T. Challenges to Developing Materials for the Transport and Storage of Hydrogen. *Nat. Chem.* **2022**, *14*, 1214–1223. [CrossRef] [PubMed]
5. Hirscher, M.; Yartys, V.A.; Baricco, M.; Bellosta von Colbe, J.; Blanchard, D.; Bowman, R.C.; Broom, D.P.; Buckley, C.E.; Chang, F.; Chen, P.; et al. Materials for Hydrogen-Based Energy Storage – Past, Recent Progress and Future Outlook. *J. Alloys Compd.* **2020**, *827*, 153548. [CrossRef]
6. Dematteis, E.M.; Berti, N.; Cuevas, F.; Latroche, M.; Baricco, M. Substitutional Effects in TiFe for Hydrogen Storage: A Comprehensive Review. *Mater. Adv.* **2021**, *2*, 2524–2560. [CrossRef]
7. Cohen, R.L.; West, K.W.; Wernick, J.H. Degradation of LaNi5 by Temperature-Induced Cycling. *J. Common Met.* **1980**, *73*, 273–279. [CrossRef]
8. Schlapbach, L.; Riesterer, T. The Activation of FeTi for Hydrogen Absorption. *Appl. Phys. Solids Surf.* **1983**, *32*, 169–182. [CrossRef]
9. Yeh, J.-W.; Chen, S.-K.; Lin, S.-J.; Gan, J.-Y.; Chin, T.-S.; Shun, T.-T.; Tsau, C.-H.; Chang, S.-Y. Nanostructured High-Entropy Alloys with Multiple Principal Elements: Novel Alloy Design Concepts and Outcomes. *Adv. Eng. Mater.* **2004**, *6*, 299–303. [CrossRef]
10. Cantor, B.; Chang, I.T.H.; Knight, P.; Vincent, A.J.B. Microstructural Development in Equiatomic Multicomponent Alloys. *Mater. Sci. Eng. A* **2004**, *375–377*, 213–218. [CrossRef]
11. Gao, M.C.; Yeh, J.-W.; Liaw, P.K.; Zhang, Y. *Hig-Entropy Alloys Fundamentals and Applications*; Springer: Berlin/Heidelberg, Germany, 2016; Volume 10, ISBN 978-3-319-27011-1.
12. Miracle, D.B. High Entropy Alloys as a Bold Step Forward in Alloy Development. *Nat. Commun.* **2019**, *10*, 1805. [CrossRef] [PubMed]
13. Yang, X.; Zhang, Y. Prediction of High-Entropy Stabilized Solid-Solution in Multi-Component Alloys. *Mater. Chem. Phys.* **2012**, *132*, 233–238. [CrossRef]
14. Guo, S.; Ng, C.; Lu, J.; Liu, C.T. Effect of Valence Electron Concentration on Stability of Fcc or Bcc Phase in High Entropy Alloys. *J. Appl. Phys.* **2011**, *109*, 103505. [CrossRef]

15. Sahlberg, M.; Karlsson, D.; Zlotea, C.; Jansson, U. Superior Hydrogen Storage in High Entropy Alloys. *Sci. Rep.* **2016**, *6*, 36770. [CrossRef] [PubMed]
16. Marques, F.; Balcerzak, M.; Winkelmann, F.; Zepon, G.; Felderhoff, M. Review and Outlook on High-Entropy Alloys for Hydrogen Storage. *Energy Environ. Sci.* **2021**, *14*, 5191–5227. [CrossRef]
17. Kong, L.; Cheng, B.; Wan, D.; Xue, Y. A Review on BCC-Structured High-Entropy Alloys for Hydrogen Storage. *Front. Mater.* **2023**, *10*. [CrossRef]
18. Sakaki, K.; Kim, H.; Asano, K.; Nakamura, Y. Hydrogen Storage Properties of Nb-Based Solid Solution Alloys with a BCC Structure. *J. Alloys Compd.* **2020**, *820*, 153399. [CrossRef]
19. Montero, J.; Ek, G.; Sahlberg, M.; Zlotea, C. Improving the Hydrogen Cycling Properties by Mg Addition in Ti-V-Zr-Nb Refractory High Entropy Alloy. *Scr. Mater.* **2021**, *194*, 113699. [CrossRef]
20. Montero, J.; Ek, G.; Laversenne, L.; Nassif, V.; Sahlberg, M.; Zlotea, C. How 10 At% Al Addition in the Ti-V-Zr-Nb High-Entropy Alloy Changes Hydrogen Sorption Properties. *Molecules* **2021**, *26*, 2470. [CrossRef]
21. Bouzidi, A.; Laversenne, L.; Nassif, V.; Elkaim, E.; Zlotea, C. Hydrogen Storage Properties of a New Ti-V-Cr-Zr-Nb High Entropy Alloy. *Hydrogen* **2022**, *3*, 270–284. [CrossRef]
22. Bouzidi, A.; Laversenne, L.; Zepon, G.; Vaughan, G.; Nassif, V.; Zlotea, C. Hydrogen Sorption Properties of a Novel Refractory Ti-V-Zr-Nb-Mo High Entropy Alloy. *Hydrogen* **2021**, *2*, 399–413. [CrossRef]
23. Montero, J.; Ek, G.; Laversenne, L.; Nassif, V.; Zepon, G.; Sahlberg, M.; Zlotea, C. Hydrogen Storage Properties of the Refractory Ti–V–Zr–Nb–Ta Multi-Principal Element Alloy. *J. Alloys Compd.* **2020**, *835*, 155376. [CrossRef]
24. Montero, J.; Zlotea, C.; Ek, G.; Crivello, J.-C.; Laversenne, L.; Sahlberg, M. TiVZrNb Multi-Principal-Element Alloy: Synthesis Optimization, Structural, and Hydrogen Sorption Properties. *Molecules* **2019**, *24*, 2799. [CrossRef] [PubMed]
25. Zlotea, C.; Bouzidi, A.; Montero, J.; Ek, G.; Sahlberg, M. Compositional Effects on the Hydrogen Storage Properties in a Series of Refractory High Entropy Alloys. *Front. Energy Res.* **2022**, *10*, 991447. [CrossRef]
26. SI Chemical Data, Third Edition (Aylward, Gordon; Findlay, Tristan) | Journal of Chemical Education. Available online: https://pubs.acs.org/doi/abs/10.1021/ed072pA109.1 (accessed on 23 June 2021).
27. Couzinié, J.P.; Dirras, G.; Perrière, L.; Chauveau, T.; Leroy, E.; Champion, Y.; Guillot, I. Microstructure of a Near-Equimolar Refractory High-Entropy Alloy. *Mater. Lett.* **2014**, *126*, 285–287. [CrossRef]
28. Silva, B.H.; Zlotea, C.; Champion, Y.; Botta, W.J.; Zepon, G. Design of TiVNb-(Cr, Ni or Co) Multicomponent Alloys with the Same Valence Electron Concentration for Hydrogen Storage. *J. Alloys Compd.* **2021**, *865*, 158767. [CrossRef]
29. Fukai, Y. The Metal-Hydrogen System. Springer-Verlag.: Berlin/Heidelberg, Germany, 2005; Volume 21.
30. Nygård, M.M.; Fjellvåg, Ø.S.; Sørby, M.H.; Sakaki, K.; Ikeda, K.; Armstrong, J.; Vajeeston, P.; Sławiński, W.A.; Kim, H.; Machida, A.; et al. The Average and Local Structure of TiVCrNbDx (X=0,2.2,8) from Total Scattering and Neutron Spectroscopy. *Acta Mater.* **2021**, *205*, 116496. [CrossRef]
31. Pineda-Romero, N.; Witman, M.; Stavila, V.; Zlotea, C. The Effect of 10 at.% Al Addition on the Hydrogen Storage Properties of the Ti0.33V0.33Nb0.33 Multi-Principal Element Alloy. *Intermetallics* **2022**, *146*, 107590. [CrossRef]
32. Nygård, M.M.; Sławiński, W.A.; Ek, G.; Sørby, M.H.; Sahlberg, M.; Keen, D.A.; Hauback, B.C. Local Order in High-Entropy Alloys and Associated Deuterides – a Total Scattering and Reverse Monte Carlo Study. *Acta Mater.* **2020**, *199*, 504–513. [CrossRef]
33. Lilensten, L.; Couzinié, J.-P.; Perrière, L.; Hocini, A.; Keller, C.; Dirras, G.; Guillot, I. Study of a Bcc Multi-Principal Element Alloy: Tensile and Simple Shear Properties and Underlying Deformation Mechanisms. *Acta Mater.* **2018**, *142*, 131–141. [CrossRef]
34. Couzinié, J.-P.; Lilensten, L.; Champion, Y.; Dirras, G.; Perrière, L.; Guillot, I. On the Room Temperature Deformation Mechanisms of a TiZrHfNbTa Refractory High-Entropy Alloy. *Mater. Sci. Eng. A* **2015**, *645*, 255–263. [CrossRef]
35. Edalati, P.; Floriano, R.; Mohammadi, A.; Li, Y.; Zepon, G.; Li, H.-W.; Edalati, K. Reversible Room Temperature Hydrogen Storage in High-Entropy Alloy TiZrCrMnFeNi. *Scr. Mater.* **2020**, *178*, 387–390. [CrossRef]
36. Vaughan, G.B.M.; Baker, R.; Barret, R.; Bonnefoy, J.; Buslaps, T.; Checchia, S.; Duran, D.; Fihman, F.; Got, P.; Kieffer, J.; et al. ID15A at the ESRF – a Beamline for High Speed Operando X-Ray Diffraction, Diffraction Tomography and Total Scattering. *J. Synchrotron Radiat.* **2020**, *27*, 515–528. [CrossRef] [PubMed]
37. Kieffer, J.; Petitdemange, S.; Vincent, T. Real-Time Diffraction Computed Tomography Data Reduction. *J. Synchrotron Radiat.* **2018**, *25*, 612–617. [CrossRef]
38. Ashiotis, G.; Deschildre, A.; Nawaz, Z.; Wright, J.P.; Karkoulis, D.; Picca, F.E.; Kieffer, J. The Fast Azimuthal Integration Python Library: *PyFAI*. *J. Appl. Crystallogr.* **2015**, *48*, 510–519. [CrossRef]
39. Juhás, P.; Farrow, C.L.; Yang, X.; Knox, K.R.; Billinge, S.J.L. Complex Modeling: A Strategy and Software Program for Combining Multiple Information Sources to Solve Ill Posed Structure and Nanostructure Inverse Problems. *Acta Crystallogr. Sect. Found. Adv.* **2015**, *71*, 562–568. [CrossRef]
40. Farrow, C.L.; Juhas, P.; Liu, J.W.; Bryndin, D.; Božin, E.S.; Bloch, J.; Proffen, T.; Billinge, S.J.L. PDFfit2 and PDFgui: Computer Programs for Studying Nanostructure in Crystals. *J. Phys. Condens. Matter* **2007**, *19*, 335219. [CrossRef]
41. Rodríguez-Carvajal, J. Recent Advances in Magnetic Structure Determination by Neutron Powder Diffraction. *Phys. B Condens. Matter* **1993**, *192*, 55–69. [CrossRef]
42. Cheary, R.W.; Coelho, A.A.; Cline, J.P. Fundamental Parameters Line Profile Fitting in Laboratory Diffractometers. *J. Res. Natl. Inst. Stand. Technol.* **2004**, *109*, 1. [CrossRef]

43. Coelho, A.A. TOPAS and TOPAS-Academic: An Optimization Program Integrating Computer Algebra and Crystallographic Objects Written in C++. *J. Appl. Crystallogr.* **2018**, *51*, 210–218. [CrossRef]
44. Gross, K.J.; Hardy, B.; Parilla, P.A. *Recommended Best Practices for Characterizing Engineering Properties of Hydrogen Storage Materials*; National Renewable Energy Laboratory: Golden, CO, USA, 2013.
45. Broom, D.P.; Hirscher, M. Irreproducibility in Hydrogen Storage Material Research. *Energy Environ. Sci.* **2016**, *9*, 3368–3380. [CrossRef]